Small Structures

small structures

www.small-structures.com

RESEARCH ARTICLE OPEN ACCESS

Single-Step Continuous-Flow Strain Engineering of Multiphase Titanate–TiO_2-Reduced Graphene Oxide Nanocomposites for Dual Photo- and Mechanocatalytic Activity

Kiem G. Nguyen[1] | Matej Huš[2] | Ana Oberlintner[2] | Ioan-Alexandru Baragau[3] | Dana G. Popescu[3] | Daniel Gherca[4] | Adela Nicolaev[3] | Tobias Heil[5] | Muhammad Tariq Sajjad[1] | Steve Dunn[1] | Conor Davids[1] | Suela Kellici[1]

[1]School of Engineering and Design, London South Bank University, London, UK | [2]National Institute of Chemistry, Ljubljana, Slovenia | [3]National Institute of Materials Physics, Ilfov, Romania | [4]National Institute of Research and Development for Technical Physics, Iasi, Romania | [5]Max-Planck Institute for Solid State Research, Stuttgart, Germany

Correspondence: Suela Kellici (kellicis@lsbu.ac.uk)

Received: 18 November 2025 | **Revised:** 6 May 2026 | **Accepted:** 1 June 2026

Keywords: continuous hydrothermal flow synthesis | density functional theory | mechanocatalysis | photocatalysis | reduced graphene oxide | strain engineering | titanate–TiO_2 heterostructures

ABSTRACT

Strain engineering is an effective strategy to tune the electronic structure and catalytic performance of functional materials. Here, we demonstrate a single-step continuous hydrothermal flow synthesis (CHFS) that produces multiphase titanate-TiO_2-reduced graphene oxide (rGO) nanocomposites capable of both photocatalytic and mechanocatalytic activity. In this approach, in situ KOH-mediated reduction of graphene oxide introduces interfacial lattice strain and directs the co-crystallisation of anatase TiO_2, layered $K_2Ti_4O_9$, and metastable TiO_2(B). The resulting multiphase composites feature strain gradients and nanoscale heterojunctions that enhance visible-light absorption, charge separation, and mechanically assisted catalytic response. Density functional theory (DFT) simulations confirm strain-induced bandgap narrowing and charge redistribution at oxide–2D interfaces. Under simultaneous visible-light irradiation and mechanical stirring, these hybrids achieved near-complete degradation of concentrated aqueous methylene blue (0.04 mM) within 60 min, with an apparent dual-mode rate constant of 0.1046 min^{-1}, outperforming conventional photocatalysts. This single-step, scalable platform provides a general route to design multifunctional catalysts for environmental remediation and solar-to-chemical energy conversion.

1 | Introduction

The development of next-generation catalytic materials demands more than compositional optimisation; it requires precise control over structure–function relationships at the atomic scale. One of the most effective tools to achieve this is strain engineering, a strategy capable of modifying electronic band structure, enhancing charge-carrier separation, and stabilising active surface states, all without altering the chemical composition of the host lattice [1–3]. However, scalable methods to embed functional strain directly into solution-processed nanomaterials, avoiding epitaxial growth or post-synthetic treatments, remain scarce [4].

Here, we present a rational strain-engineering framework enabled by a rapid, one-step synthesis platform: continuous hydrothermal flow synthesis (CHFS) [5–7]. In contrast to conventional batch hydrothermal methods, CHFS uses supercritical water (≥374°C, >22 MPa) under dynamic flow conditions to drive near-instantaneous nucleation and crystallisation. This

highly non-equilibrium environment stabilises metastable and layered oxide phases [8], inherently generating internal strain through mismatches in thermal expansion, phase asymmetry, and interfacial coupling [9]. By introducing strain in situ during synthesis, CHFS provides a scalable, chemically versatile strategy for tailored structural and electronic tuning [10].

To demonstrate this concept, we designed a TiO_2-based multiphase oxide–carbon nanocomposite in which strain emerges naturally from the coexistence of compositionally and structurally distinct domains. Titanium dioxide (TiO_2) was selected as the model oxide platform owing to its well-established photocatalytic performance and structural polymorphism, which make it particularly responsive to phase and strain-directed tuning [11]. Reduced graphene oxide (rGO) served as both a charge-extracting scaffold and a mechanical modulator, inducing interfacial strain via mismatch in thermal and structural properties [12]. Under controlled CHFS conditions with KOH as a reducing agent, this coupling directed the selective formation of metastable TiO_2(B) and layered $K_2Ti_4O_9$, both known for their anisotropic charge transport characteristics [13]. Systematic variation of rGO loading revealed its multifunctional role: in addition to acting as an electron acceptor, rGO serves as a strain-inducing and phase-directing template that influences the composite's polymorphic outcome.

In this single-step process, KOH was employed as a dual-function reagent: it guided oxide phase crystallisation and simultaneously reduced graphene oxide in situ. This approach replaces the previous use of ammonia [10] and enables direct formation of a fully integrated heterostructure. The result is a complex, yet highly ordered nanocomposite featuring strain gradients, layered domains, and strong interfacial electronic coupling, all of which underpin its catalytic functionality.

Comprehensive structural and electronic characterisation (XRD, HRTEM, Raman, UPS, UV–vis DRS, transient PL), together with first-principles modelling, confirmed strain-driven bandgap narrowing, interfacial charge redistribution, and extended carrier lifetimes. Photocatalytic activity was evaluated through degradation of a concentrated model dye (0.04 mM), with the degradation mechanism investigated using EPR spectroscopy. Under visible light irradiation with simultaneous mechanical stirring, complete dye degradation was achieved in 60 min, corresponding to an exceptionally high first-order rate constant of 0.1046 min^{-1}. Remarkably, even under mechanical excitation alone, the material retained significant catalytic activity, reaching ~40% degradation ($k = 5.57 \times 10^{-3}$ min^{-1} at 550 rpm), indicating that interfacial strain may facilitate charge activation through non-photonic, mechanically driven pathways analogous to piezocatalysis [14, 15].

Overall, this study introduces a generalisable strategy for synthesising strain-activated photocatalytic materials. By uniting rapid, flow-based processing with interfacial strain engineering and metastable phase control, we establish a scalable route to multifunctional catalysts that respond to both solar and mechanical energy inputs. This approach opens a pathway to more versatile materials design, adaptable across environmental remediation and broader energy-conversion technologies [16].

2 | Results and Discussion

To translate our design framework into functional performance, we synthesised a series of TiO_2-based nanocomposites using continuous hydrothermal flow synthesis (CHFS), a rapid and scalable platform for delivering structural and compositional complexity. By systematically varying graphene oxide content, we directed the selective crystallisation of metastable TiO_2(B) and layered $K_2Ti_4O_9$ within an anatase-rich matrix. These phases, embedded within a reduced graphene oxide (rGO) scaffold, formed extended heterointerfaces characterised by lattice mismatch and localised strain. Structural, spectroscopic, and electronic characterisation revealed strong correlations between rGO loading, phase composition, and band-edge modulation, establishing strain as a tunable design parameter. We next assessed catalytic behaviour under simulated solar irradiation ($\lambda \geq 400$ nm), mechanical, and combined excitation to probe how these features govern dual-mode activation in high-performance catalytic materials.

For clarity, three reference labels are used throughout this work. TiO_2–CHFS denotes the anatase-only sample synthesised without KOH or GO and is used solely as the unstrained Raman reference. TiO_2 denotes the multiphase control synthesised with KOH but without GO and is the catalytic control discussed in the main text. TiO_2–rGO–x denotes the KOH-mediated multiphase composites prepared with an initial GO concentration of x mg mL^{-1} in the precursor feed.

2.1 | Structure, Morphology, and Surface Chemistry of the Nanocomposites

Powder X-ray diffraction (XRD) confirms that the CHFS products comprise a multiphase oxide matrix. The diffraction patterns (Figure 1a–d) show peaks for tetragonal anatase TiO_2, monoclinic TiO_2(B), layered $K_2Ti_4O_9$, and a broad feature from the hexagonal rGO scaffold. Increasing the GO loading in the precursor systematically alters the phase composition: higher rGO content promotes the formation of TiO_2(B) and $K_2Ti_4O_9$ at the expense of anatase. This trend is attributed to templating effects of the 2D-rGO, whose high surface area and morphology influence nucleation kinetics. Le Bail refinements of the XRD data corroborate these phase assignments and show changes in lattice parameters and peak broadening indicative of internal strain (Figure S1, S2, and Table S1).

The coexistence of anatase and TiO_2(B) phases promotes heterophase junctions that facilitate charge separation and suppress electron–hole recombination to improve photocatalytic efficiency [17]. Synthesising this biphasic mixture is challenging because TiO_2(B) is metastable and typically requires prolonged reaction times [18]. CHFS overcomes these limitations by enabling instantaneous nucleation and rapid phase evolution. Although anatase is the thermodynamic product, the presence of KOH and GO in the synthesis promotes the formation and stabilisation of TiO_2(B), consistent with a sequential pathway: titanium(IV) bis(ammonium lactato) dihydroxide reacts with KOH to form potassium titanates, which convert to hydrogen titanates and subsequently dehydrate into TiO_2(B) [19]. A fraction of TiO_2(B) transforms to anatase at reaction

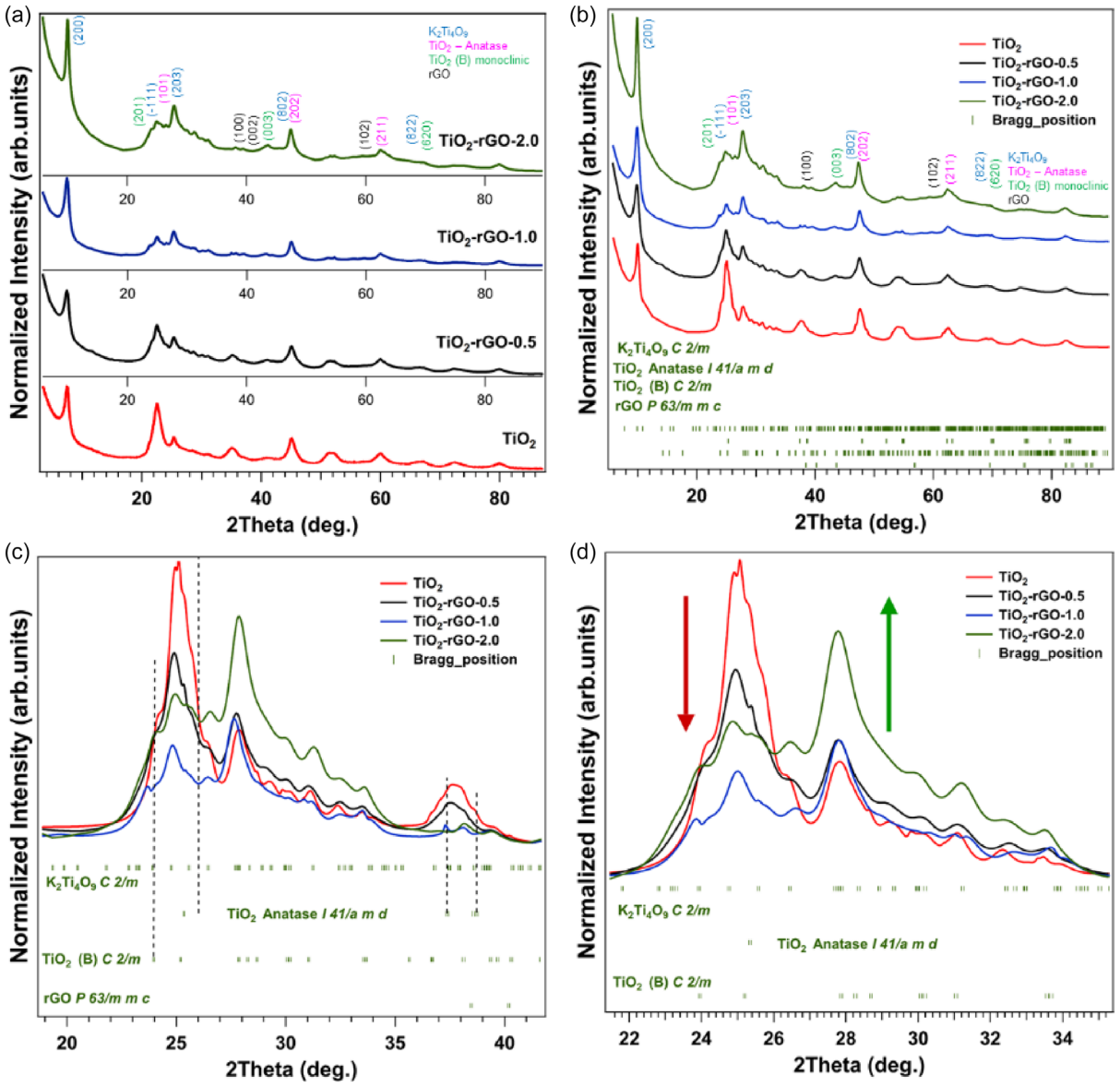

FIGURE 1 | (a) Powder X-ray diffraction patterns of the synthesised nanocomposites; (b) Superimposed XRD patterns with identified crystalline phases: monoclinic $K_2Ti_4O_9$ (C2/m), tetragonal anatase TiO_2 ($I4_1/amd$), monoclinic TiO_2(B) (C2/m), and hexagonal rGO ($P6_3/mmc$); (c) Zoomed-in view of the 2θ range from 19° to 42°, highlighting variations in peak intensity and broadening as a function of synthetic conditions. (d) Superimposed X-ray diffraction patterns enabling direct comparison of crystallographic phases and relative peak intensities among the synthesised samples. Key: TiO_2 = multiphase anatase/TiO_2(B)/$K_2Ti_4O_9$.

temperature, while GO critically governs the resulting phase distribution [20].

The phase composition, modulated by GO content and alkalinity, dictates interfacial strain and heterojunction density (Table S1). GO induces phase-selective lattice strain, most pronounced in anatase (sample TiO_2-rGO-0.5, $\varepsilon_{XRD} = 33.2 \times 10^{-3}$), and decreases at higher GO loadings. Unit-cell refinements indicate minor a-axis expansion and c-axis contraction, consistent with interfacial densification. $K_2Ti_4O_9$ remains weakly strained up to 1.0 mg mL^{-1} GO but exhibits a marked increase at higher GO loadings ($\varepsilon_{XRD} = 216.5 \times 10^{-3}$), confirming interface-driven distortion. TiO_2 (B) likely accommodates early lattice strain, though its low intensity precluded quantitative analysis. Raman spectroscopy provides complementary insight into local vibrational strain within anatase.

High-resolution transmission electron microscopy (HRTEM) provides direct evidence of the multiphase architecture and interfacial strain in CHFS-derived composites. The images (Figure 2) display distinct lattice fringes corresponding to TiO_2(B) (001, 0.63 nm) [21] and $K_2Ti_4O_9$ (200, 0.88 nm), confirming the coexistence of these phases [22]. TiO_2 nanoparticles ranging from 3–11 nm (mean 6.5 ± 2.0 nm) are uniformly distributed on rGO sheets, reflecting growth suppression and surface templating under CHFS supersaturation [23]. The coexistence of TiO_2 phases with non-matching lattice parameters generates interfacial strain, while lattice defects and dislocations localise additional distortion fields [24]. Comparative HRTEM of TiO_2 anatase (Figure 3a) exhibits well-defined (101, 0.35 nm), (110, 0.32 nm), and (002, 0.19 nm) planes, whereas TiO_2–rGO composites (Figure 3b,c) show fringe distortion and lattice curvature (green arrows), resulting from rapid CHFS nucleation and

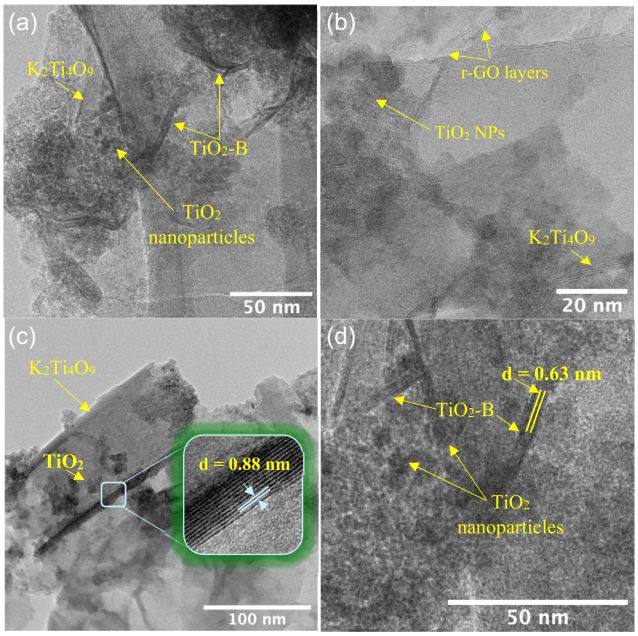

FIGURE 2 | (a) TEM image of the TiO_2 nanocomposite showing anatase nanoparticles, rod-like TiO_2(B), and $K_2Ti_4O_9$; (b) representative morphology of TiO_2–rGO nanocomposites; (c) HRTEM image highlighting lattice fringes of $K_2Ti_4O_9$; (d) lattice spacing corresponding to TiO_2 (B), confirming phase identification.

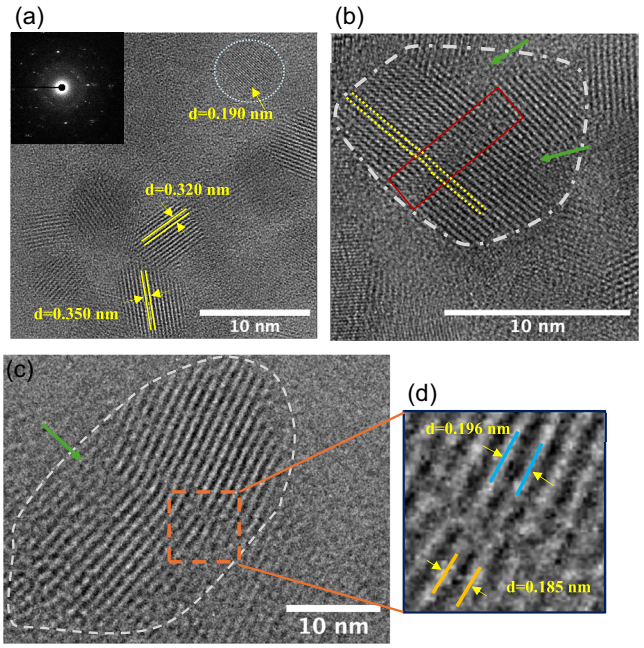

FIGURE 3 | (a) HRTEM image of pristine TiO_2 nanoparticles showing lattice fringes and particle size distribution ($n = 150$); (b,c) representative HRTEM micrographs of TiO_2–rGO nanocomposites highlighting local lattice distortion induced by interfacial strain; (d) variation in d-spacing across nanoparticles, evidencing strain-modulated structural deformation. Regions marked in red and blue represent compressed and expanded lattice, respectively; green arrows indicate distorted fringes and lattice irregularities.

interface-mediated growth. Measured d-spacings vary from 0.185 nm (compressed) to 0.196 nm (expanded) (Figure 3d), demonstrating tensile–compressive strain asymmetry across crystallites. These atomic-scale distortions correlate with XRD-derived microstrain (Table S1), establishing interfacial strain as an intrinsic structural feature of the nanocomposite framework. Additional HRTEM images are shown in Figure S3.

Raman spectroscopy provides further insights into local strain and phase composition (Figure 4). All samples displayed the four characteristic vibrational modes of anatase TiO_2. In the unstrained reference sample (TiO_2-CHFS synthesised without any KOH or GO), the primary E_g mode appeared sharply at 146.6 cm^{-1} (with a full width at half maximum, FWHM, of 19.06 cm^{-1}). Upon rGO incorporation, this peak exhibited a systematic blueshift and broadening (155.1 cm^{-1}, FWHM = 26.67 cm^{-1}) in TiO_2–rGO–2.0 indicative of increasing compressive strain and phonon confinement (Figure S4). Strain values (ε) calculated from the E_g shift (ca. 146.6 cm^{-1}) (Table S2) showed a monotonic increase with rGO loading, correlating with microstrain (ε_{XRD}) extracted from XRD Rietveld analysis (Table S3), confirming the presence of lattice distortion induced by interfacial mismatch between TiO_2 and rGO. TiO_2(B), though weakly Raman-active [25], was supported by a band near 280.7 cm^{-1} and by broadening of the B_{1g} mode at ~396 cm^{-1}, likely due to overlap with E_g vibration near 440 cm^{-1}. Ti—O vibrations in layered $K_2Ti_4O_9$, consistent with XRD results and the expected vibrational range of titanate frameworks, were also present. The D (~1340 cm^{-1}) and G (~1580 cm^{-1}) bands of rGO were observed in all reduced samples. The I_D/I_G ratios remained consistent (~1.1 confirming moderate defect density).

The XPS survey spectra (Figure S5) confirm the presence of Ti, O, K, and C, consistent with rGO incorporation and potassium titanate formation. Potassium was identified via the K_{2p} doublet at ~293.1 eV, consistent with potassium titanate phase also observed in XRD [26]. The O1s spectra exhibit a dominant peak at ~530.0 eV attributable to lattice oxygen in Ti-O bonds, accompanied by a pronounced shoulder at ~531.5–532.5 eV arising from surface hydroxyl groups and oxygenated carbon functionalities, reflecting the complex and heterogeneous surface chemistry of the TiO_2-rGO nanocomposites. High-resolution Ti_{2p} spectra (Figure S6) revealed characteristic Ti^{4+} $2p_{3/2}$ and $2p_{1/2}$ peaks at 458.3 eV and 464.2 eV in the TiO_2 [27], indicative of stoichiometric TiO_2. Ti^{3+} states (~456.8 eV) [28], which increased with GO loading, were also observed. These Ti^{3+} features suggest oxygen vacancy formation or partial reduction of Ti^{4+} species facilitated by alkaline conditions in the CHFS reducing environment. These defects can contribute to bandgap narrowing and improved conductivity. Deconvolution of the C1s spectra demonstrated a dominant sp^2 carbon peak (~284.6 eV) accompanied by oxygenated species attributed to C—O (~285.7 eV), C═O (~286.8 eV), and O—C═O (~288.6 eV) functionalities [29]. Notably, TiO_2–rGO–2.0 exhibited additional low binding energy carbon features at 281.9 eV and 283.0 eV, consistent with strong interfacial Ti—C/Ti—O—C coupling [30], indicative of chemical coupling at the rGO-TiO_2 interface. This interfacial bonding is expected to facilitate charge transfer across the TiO_2-rGO interface.

Quantitative elemental analysis (Table S4) shows the Ti/K ratio decreases with more GO, (consistent with more $K_2Ti_4O_9$ phase), and the C content increases as expected. These trends mirror the XRD phase evolution. Complementing these results, FTIR analysis (Figure S7) also demonstrates substantial reduction of

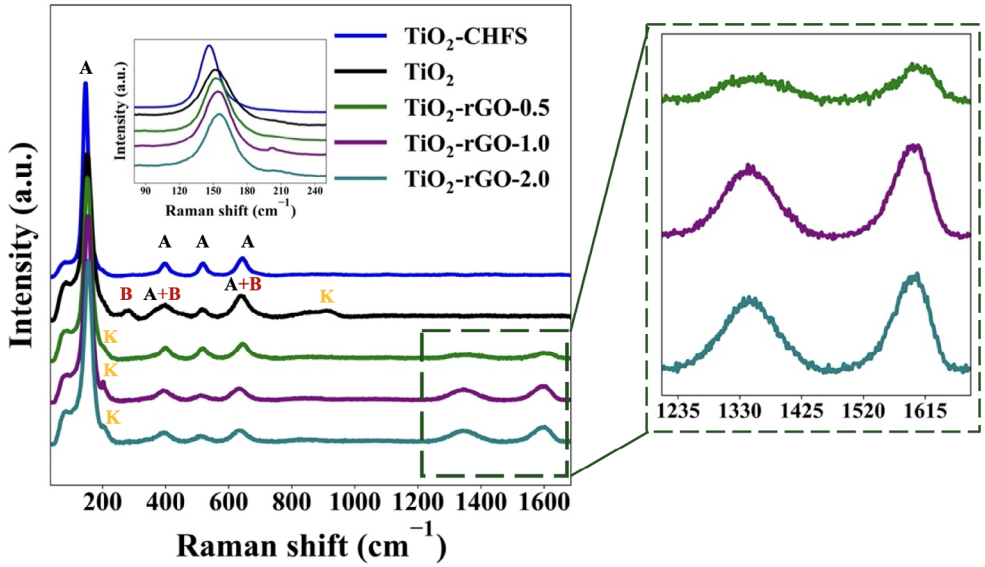

FIGURE 4 | Raman spectra of pristine TiO_2 - CHFS and nanocomposites, showing characteristic modes of anatase (A), TiO_2(B), and $K_2Ti_4O_9$ (K). The E_g mode exhibits a progressive blueshift and broadening with rGO addition, indicating increasing compressive strain. Inset (a): E_g peak shift (∼145–155 cm^{-1}) used for strain analysis. Inset (b): D (∼1340 cm^{-1}) and G (∼1580 cm^{-1}) bands confirm successful rGO incorporation.

oxygenated groups in TiO_2-rGO compared to pristine GO. The broad O—H band (3000–3500 cm^{-1}) in GO is significantly weakened in TiO_2 and TiO_2-rGO during CHFS synthesis [31]. The disappearance of the 1030 cm^{-1} C—O stretching peak, and attenuation of carboxyl and epoxy-related bands (1430 and 1220 cm^{-1}) further confirm GO reduction [32]. A Ti—O—Ti vibration near 800 cm^{-1} is observed in both TiO_2 and TiO_2-rGO, with a slight redshift in the latter suggesting Ti—O—C bond formation [33]. Thermogravimetric analysis was also undertaken (Figure S17), confirming the level of reduction of the rGO as measured by XPS.

2.2 | Optical and Electronic Structure of the Nanocomposites

Analysis of diffuse reflectance spectra (Figures 5, and S8 & 9) shows a progressive narrowing of bandgaps with increasing GO content. This reflects a gradual perturbation of the electronic structure, driven by interfacial strain, the formation of Ti^{3+} defect states, and the appearance of Ti—C and Ti—O—C interfacial bonding, as confirmed by XPS, FTIR, and DFT results.

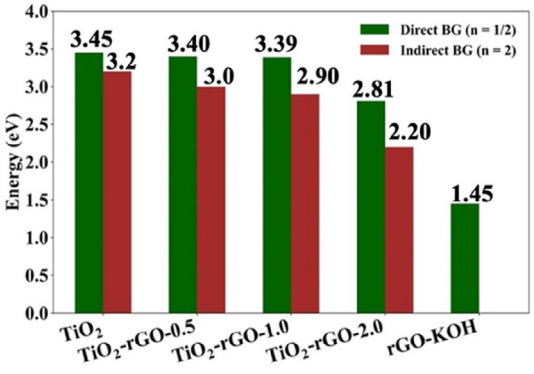

FIGURE 5 | Direct and indirect optical bandgaps of synthesised multiphase TiO_2 nanocomposites, showing progressive narrowing with increasing GO content.

These features introduce localised sub-bandgap states, extending the optical response into the visible region. Bandgap narrowing in the TiO_2-rGO-2.0 sample is particularly pronounced. All nanocomposites exhibit a multiphase oxide matrix comprising anatase, TiO_2(B), and $K_2Ti_4O_9$, each contributing distinct band edge positions and redox properties [34].

Ultraviolet photoemission spectroscopy (UPS, Figure S10) reveals systematic shifts in valence band maximum (VBM) and conduction band minimum (CBM) across the series, demonstrating strong electronic coupling between the oxide phases and the carbon scaffold. Literature reports show that $K_2Ti_4O_9$ exhibits a VBM/CBM of +3.06 V/−0.48 V, providing a strong oxidative potential favouring ROS generation [35]. Anatase (+2.67 V/−0.53 V) and monoclinic TiO_2(B) (+2.34 V/−0.56 V) provide complementary redox behaviour [36]. rGO rapidly extracts electrons through Ti-C interfacial interactions and its conductive π-network [37] suppressing charge recombination. These synergistic effects account for the longer carrier lifetimes observed in time-resolved photoluminescence (PL) decay (Figure 6) and underpin the enhanced photocatalytic performance of the strain-engineered composites.

The average lifetime (τ_{avg}) was determined using the intensity weighted average of fitted multiple exponentials (Equation (2) [5], with detailed parameters summarised in Table S5. Incorporation of rGO produces a clear increase in carrier lifetime, from ca. 19 ns for the multiphase TiO_2 sample to about 27 ns for TiO_2-rGO-2.0, indicating more efficient suppression of electron–hole recombination. This correlates with the trend in photocatalytic efficiency, confirming that longer-lived charges indeed translate to better reaction performance. The longer lifetime originates from strong electronic coupling at the oxide–carbon interface, where rGO serves as a conductive sink for photogenerated

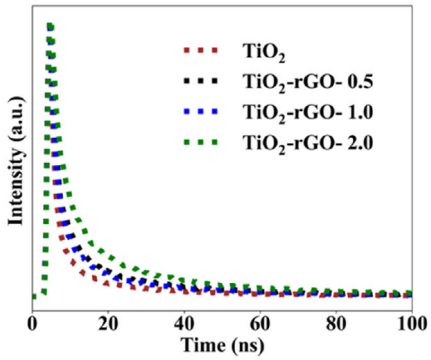

FIGURE 6 | Time-resolved photoluminescence decays of the synthesised multiphase TiO_2 and TiO_2-rGO nanocomposites.

electrons. The formation of interfacial Ti—C and Ti—O—C bonds facilitate charge delocalisation and stabilise the charge-separated state. These lifetime enhancements also correlate with the interfacial strain signatures observed experimentally, suggesting that strain fields arising from lattice mismatch modulate band curvature and carrier mobility, further promoting charge transport.

Furthermore, to complement the experimental results, density functional theory (DFT) calculations were performed to provide insight into how rGO incorporation and applied strain influence the electronic structure of the composites. The calculated bandgaps for anatase, monoclinic TiO_2, and $K_2Ti_4O_9$ semiconductors are 3.18, 3.82, and 4.17 eV, respectively, whereas reduced graphene oxide (rGO) is nearly zero-gap. Under uniaxial strain (Figure S11), the bandgaps of these materials respond non-uniformly: those of GO/rGO increase monotonically, while TiO_2 polymorphs and $K_2Ti_4O_9$ show orientation-dependent, non-monotonic shifts due to orbital rehybridisation. This behaviour is consistent with the experimentally observed bandgap narrowing and enhanced visible-light absorption obtained from UV–vis spectroscopy, which arise from combined effects of interfacial strain, Ti^{3+} defect states, and TiO_2–rGO electronic coupling.

Interface models (Figure 7) show that lattice mismatch produces mechanical deformation in both oxide and carbon phases. Relaxed geometries yield strains of + 1.2% in anatase and 2.8% in rGO for the anatase/rGO system, and + 1.1% in $K_2Ti_4O_9$ with +0.5% in rGO for the $K_2Ti_4O_9$/rGO interface. These values are in good agreement with experimentally measured strain signatures, including XRD microstrain, Raman E_g peak shifts, and local lattice distortions observed by HRTEM, confirming that interfacial strain is an intrinsic feature of the multiphase nanocomposite (Table S3). The graphene sheet in the anatase/rGO model becomes significantly undulated to maximise contact, whereas it remains flatter on $K_2Ti_4O_9$ indicating a better lattice match with the layered titanate. This suggests strain is more localised at anatase–rGO interfaces.

Electronic-structure analysis indicates that contact with rGO lowers the anatase work function relative to the isolated slab, while the $K_2Ti_4O_9$/rGO interface exhibits a strain-dependent variation of approximately 0.04 eV per % strain (Figure 8). These calculated work-function shifts are qualitatively consistent with the UPS-derived band alignment and Fermi-level shifts, supporting interfacial charge redistribution within the TiO_2–rGO system. Interfacial charge transfer analysis further highlights subtle yet significant differences in electronic coupling: 0.0035 e^0 per carbon atom is transferred from anatase to rGO, and 0.0022 e^0 per carbon atom is found at the $K_2Ti_4O_9$/rGO interface, indicating stronger electronic coupling for anatase–rGO interactions. This interfacial charge transfer correlates with the experimentally observed increase in PL lifetimes, confirming improved charge separation and reduced recombination in rGO-containing composites.

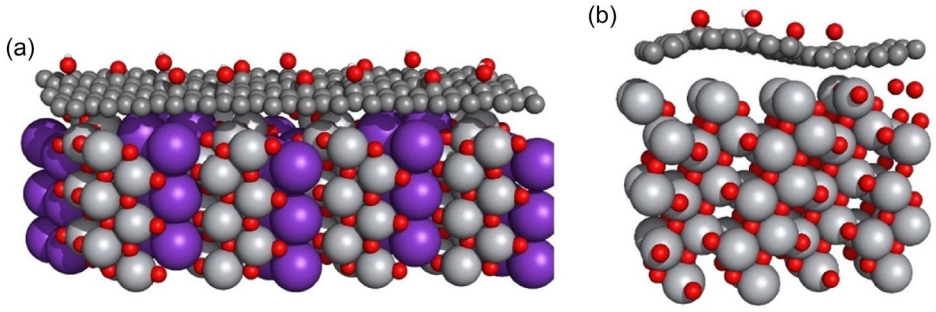

FIGURE 7 | (a) $K_2Ti_4O_9$ / rGO contact; (b) TiO_2 / rGO contact, both under most stable strain conditions.

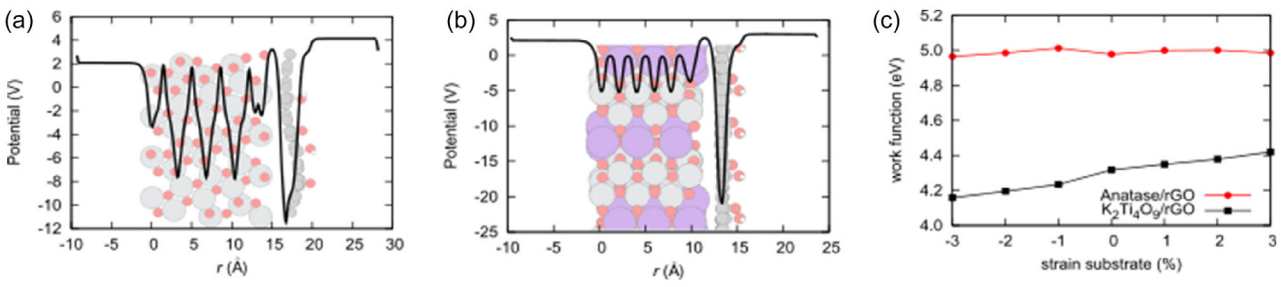

FIGURE 8 | Local potential at the (a) TiO_2 / rGO contact, (b) $K_2Ti_4O_9$ / rGO contact, and (c) the dependence of the work function on strain.

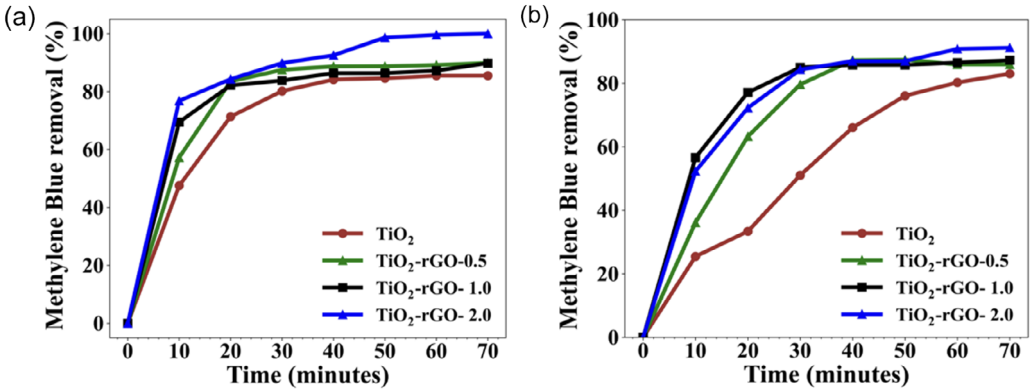

FIGURE 9 | The photocatalytic degradation of methylene blue using multiphase TiO_2 and TiO_2-rGO nanocomposites under (a) 1.0 sun and (b) 0.5 sun visible-range simulated solar irradiation.

To further probe the interfacial electronic interactions between reduced graphene oxide (rGO) and titania domains, a series of $(TiO_2)_n$ clusters ($n = 4$, 8, 12, 27, 36) were modelled on a 3×4 rGO supercell, as depicted in Figure S12. The clusters were constructed in cubic geometries to reflect anatase-like motifs. Due to the large supercell sizes and computational demand, electronic structure calculations were performed using the PBE functional. These calculations show that increasing TiO_2 domain size enhances charge transfer to rGO and lowers the work function, indicating stronger interfacial electronic coupling. The experimental results demonstrate that overall catalytic performance is governed by a combination of factors, including phase composition, strain distribution, surface area, defect density, and interfacial accessibility. Thus, while the cluster models provide insight into charge–transfer behaviour, they do not solely determine the observed activity trends.

2.3 | Photocatalytic Degradation of Methylene Blue

The photocatalytic activities of the nanocomposites were evaluated using methylene blue (0.04 mM) as a model pollutant under simulated solar irradiation ($\lambda \geq 400$ nm) at two light intensities: 1 sun (100 mW cm^{-2}) and 0.5 sun (50 mW cm^{-2}). Under sunlight intensity of 1 sun (Figure 9), all TiO_2-rGO nanocomposites achieved > 80% MB degradation within 20 min, outperforming the multiphase TiO_2 (mixed anatase/TiO_2(B)/$K_2Ti_4O_9$). Amongst the series, TiO_2-rGO-2.0 exhibited the highest activity, reducing MB to < 1% after 50 min. A control test without catalyst confirmed negligible photolysis (8.6%, Figure S13). Even under reduced intensity (0.5 sun), the rGO-based composites maintained high activity (up to 91% degradation), whereas the activity of the TiO_2 reference (anatase/TiO_2(B)-$K_2Ti_4O_9$ without rGO) declined. These improvements originate from rGO-induced bandgap narrowing, enhanced visible-light absorption, and more efficient charge separation, consistent with the optical and electronic analyses discussed above.

The reaction kinetics were analysed using the Langmuir–Hinshelwood model Equation (3), linear fits of $\ln(C/C_0$ vs. time, Figure S14) provided apparent first-order rate constants (k_{app}) (Table 1) [38]. Relative to the multiphase TiO_2 control, the rGO-modified materials displayed substantially higher reaction rates;

TABLE 1 | Apparent first-order rate constants (k_{app}) for MB degradation over nanocomposites under 1.0 sun and 0.5 sun simulated solar irradiation. Values obtained from linear fits of $\ln(C_t/C_0)$ versus t.

	Rate constant, min^{-1}	
Sample	**1 sun**	**0.5 sun**
TiO_2	0.0247	0.0253
TiO_2-rGO-0.5	0.0282	0.0269
TiO_2-rGO-1.0	0.0254	0.0248
TiO_2-rGO-2.0	0.0961	0.0329

notably, TiO_2-rGO-2.0 achieved a k_{app} nearly four times higher under full solar flux (0.0961 min^{-1} vs. 0.0247 min^{-1}). The enhancement stems from the dual function of rGO: its oxygen-containing groups supply additional adsorption sites for dye molecules, while its delocalised π-network efficiently extracts photogenerated electrons, suppressing electron–hole recombination. Together, these effects accelerate photo-oxidation and account for the superior catalytic efficiency of the rGO-integrated composites.

2.4 | Adsorption Behaviour and Strain-Dependent Surface Reactivity

The adsorption behaviour of the nanocomposites was investigated in the dark to decouple surface interactions from photochemical effects. The dye adsorption capacity (q_t, Equation (4)) is summarised in Figure 10. Incorporation of reduced graphene oxide (rGO) markedly improved the adsorption performance of TiO_2-based nanocomposites. Whereas the TiO_2 reference (anatase/TiO_2(B)/$K_2Ti_4O_9$) sample exhibited limited adsorption capacity, progressive addition of rGO led to greater dye uptake, with TiO_2-rGO-2.0 showing the most significant improvement. This improvement is attributed to the larger accessible surface area and the presence of oxygenated functional groups on rGO, which provide additional active sites for dye adsorption. BET analysis (Table S6) confirms that increasing rGO content increases the surface area from 123.7 m^2 g^{-1} for TiO_2 to 242.8 m^2 g^{-1} for TiO_2-rGO-2.0, thereby facilitating stronger surface interactions and promoting faster interfacial charge transfer during subsequent photocatalysis.

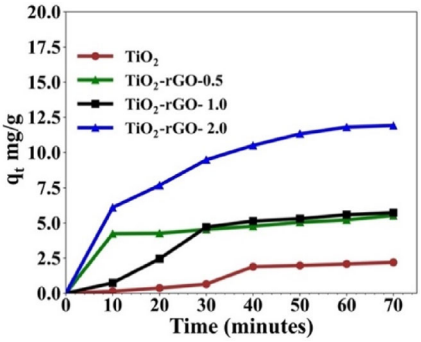

FIGURE 10 | The adsorption capacity of multiphase TiO_2 and TiO_2-rGO nanocomposites.

To elucidate the adsorption kinetics, the experimental data were fitted with both pseudo-first-order and pseudo-second-order models (Equations (5) and (6)). The former primarily describes initial physisorption, whereas the latter accounts for chemisorption processes involving electron sharing or transfer [39]. The corresponding fits are shown in Figure S15, and the extracted kinetic parameters are listed in Table S7. The TiO_2 (anatase/TiO_2(B)/$K_2Ti_4O_9$) control sample follows the pseudo-first-order model, indicating physisorption-dominated behaviour. In contrast, all multiphase TiO_2-rGO nanocomposites are best described by the pseudo–second-order model, consistent with a chemisorption process facilitated by rGO. The shift from physisorption to chemisorption is supported by higher correlation coefficients (R^2) and increased rate constants (k_2), indicating that rGO provides new active adsorption sites for MB, likely via π–π interactions or electrostatic attraction to rGO's surface functionality.

The dye degradation performance of the synthesised nanocomposites was further studied through first-principles adsorption calculations of methylene blue (MB), H*, and OH* on key components: rGO, $K_2Ti_4O_9$, and anatase TiO_2. For anatase and $K_2Ti_4O_9$, the (101) and (010) low-index facets were selected as representative surfaces [40], while rGO was modelled as a functionalised graphene sheet with hydroxyl and epoxy groups (Figure 11).

Adsorption calculations were performed under both unstrained and biaxially strained conditions, simulating compression and expansion along the *x* and *y* directions. Due to its comparatively isotropic strain response within the chosen oxygen-functionalised graphene model, rGO exhibited negligible variation in adsorption energy across strain conditions. Similarly, $K_2Ti_4O_9$ displayed only modest strain-dependent modulation: MB binding weakened slightly with expansion, while H*/OH* interactions strengthened marginally. In contrast, anatase demonstrated a pronounced anisotropic response. Strain along the *x*-axis induced a moderate decrease in adsorption strength, whereas *y*-axis expansion significantly enhanced surface affinity, particularly for polar adsorbates.

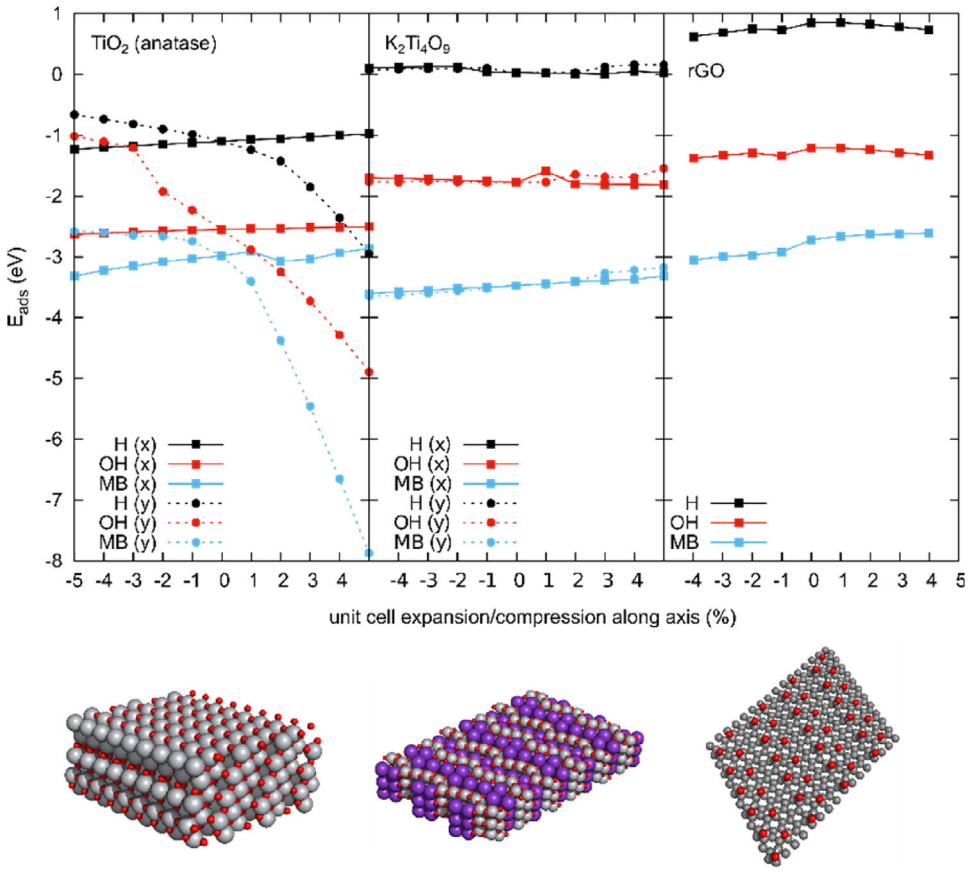

FIGURE 11 | Adsorption interaction of H*, OH*, and methylene blue (MB) with anatase TiO_2 (101), $K_2Ti_4O_9$ (010), and rGO as a function of unit cell expansion and compression.

This directional sensitivity is attributed to the inherent lattice asymmetry and polar nature of the (101) facet, offering insight into the strain-tunable reactivity of anatase-based photocatalysts. Importantly, this behaviour is consistent with the experimentally observed increase in adsorption capacity (Figure 10) and the enhanced photocatalytic degradation rates for samples with optimised rGO content and strain. In particular, the strengthened adsorption of OH^* species on strained anatase surfaces provides a favourable environment for hydroxyl-radical-related (•OH) pathways, consistent with the EPR spin-trapping results identifying •OH-type species as a dominant reactive pathway. These results suggest that moderate tensile strain in anatase enhances adsorption of key intermediates without compromising surface stability, while rGO remains largely strain-insensitive and $K_2Ti_4O_9$ exhibits only minor contributions.

2.5 | Mechanocatalysis and Photo-Mechanical Coupling

Catalytic activities were further examined under dark conditions with mechanical stirring to probe strain-driven catalysis (Figure 12). Remarkably, all composites displayed measurable activity even in the absence of light. At 250 rpm, TiO_2-rGO-0.5 and −1.0 showed significantly higher MB degradation than the TiO_2 reference (anatase/TiO_2(B)/$K_2Ti_4O_9$), confirming that mechanical excitation alone can initiate catalytic processes when strain-active interfaces are present. Thus, agitation likely induces cyclic interfacial deformation and interparticle contact, promoting charge separation and redox reactions at strain-active heterointerfaces. Increasing agitation speed enhanced the reaction rate for all samples, although TiO_2-rGO-0.5 consistently outperformed the others, with its rate constant increasing from 2.36×10^{-3} to 5.57×10^{-3} min^{-1} (Table 2). In contrast, TiO_2-rGO-2.0, initially less active, showed a threshold-like response, with a lower rate at low rpm and a modest increase at high rpm.

This behaviour mirrors the strain distribution observed structurally. TiO_2-rGO-0.5 has moderate strain, which favours reversible deformation and interfacial charge separation. At higher rGO loadings, excessive network formation disrupts long-range order, dampening mechanical responsiveness despite improved conductivity [41, 42]. The coexistence of strain-tolerant phases (e.g., $K_2Ti_4O_9$, TiO_2(B)) facilitates localised deformation but only when synergistically coupled with anatase. Together, these results demonstrate that internal strain within the TiO_2-rGO composites can be exploited for mechanically induced catalysis, operating as a complementary activation mode to light-driven photocatalysis.

TABLE 2 | Rate constants for strain-induced mechanocatalysis of methylene-blue degradation.

	Rate constant assigned at different stirring speeds ($\times 10^{-4}$ min^{-1})			
Sample	**250 rpm**	**350 rpm**	**450 rpm**	**550 rpm**
TiO_2	4.8	5.3	6.6	9.9
TiO_2-rGO-0.5	23.6	43.9	46.6	55.7
TiO_2-rGO-1.0	21.6	43.8	44.4	46.3
TiO_2-rGO-2.0	8.6	20.6	22.9	25.3

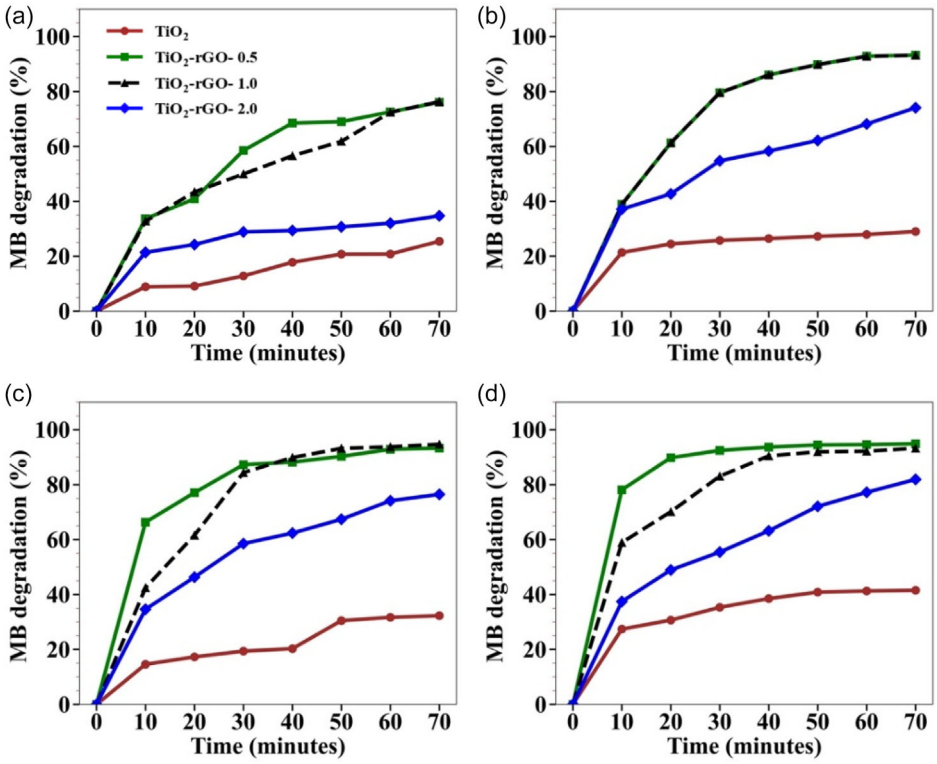

FIGURE 12 | Methylene blue degradation by multiphase TiO_2 and TiO_2-rGO nanocomposites under mechanical excitation in the dark at varied stirring speeds: (a) 250 rpm, (b) 350 rpm, (c) 450 rpm, and (d) 550 rpm, highlighting the influence of mechanical excitation on catalytic efficiency.

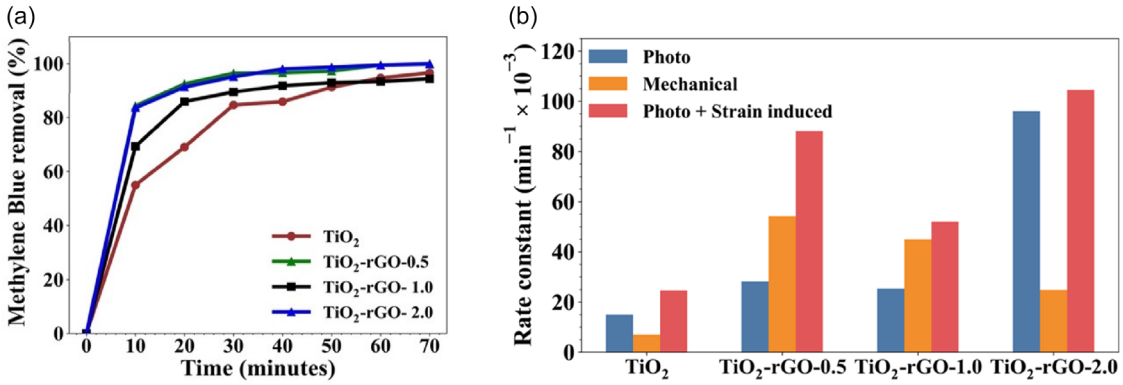

FIGURE 13 | (a) Methylene blue degradation profiles under concurrent photo–mechanical excitation (1 sun, 250 rpm) for nanocomposites; (b) corresponding apparent rate constants (k_{app}), demonstrating synergistically accelerated degradation kinetics.

The catalysts were next evaluated under simultaneous solar irradiation and mechanical stirring (250 rpm) to assess cooperative photo–mechanical activation (Figure 13). Under these conditions, all TiO_2-rGO composites exhibited enhanced performance. Rapid dye degradation occurred within the first 20 min, with the rGO-modified catalysts reaching > 90% removal considerably faster than the TiO_2 control, which achieved only ~85% removal after 70 min. The TiO_2-rGO-0.5 composite achieved nearly complete degradation within this time frame. Rate constants derived from these experiments quantify the synergy between the two stimuli: the synergy factor (S) (Table S8) is approximately 1.05 for TiO_2-rGO-0.5, indicating a positive interaction between light and mechanical effects. By contrast, TiO_2-rGO-2.0 gives S = ≈0.93, suggesting that excessive rGO coverage dampens strain transfer and limits cooperative enhancement. Detailed mode-specific degradation profiles (adsorption, photocatalysis, and mechanocatalysis) for TiO_2-rGO composites of varying rGO content are shown in Figure S16, confirming the dominant role of photonic activation and synergistic strain effects.

To distinguish intrinsic activity from surface-area effects, apparent rate constants were normalised by BET surface area (k_{norm}, min^{-1} m^{-2} g^{-1}, Table S8). The normalised values confirm that differences in performance cannot be attributed solely to surface area. Although TiO_2–rGO–2.0 shows the highest apparent rate under dual excitation, its intrinsic activity per unit surface area is comparatively modest, indicating that the improvement arises mainly from greater surface availability rather than enhanced reactivity. In contrast, TiO_2–rGO–0.5 exhibits both high apparent and high normalised rate constants, demonstrating genuine synergy between photocatalytic and mechanocatalytic processes. This composition balances accessible surface area with optimal strain and electronic coupling, making it the most efficient catalyst within the series. Additional analysis of the composites post dye-degradation was carried out via Raman and FTIR (Figure S18) to confirm the proposed mechanism and stability of the catalysts.

2.6 | Electron Paramagnetic Resonance Spin-Trapping Evidence for Reactive Oxygen Species

Electron paramagnetic resonance (EPR) spin-trapping experiments using 5,5-dimethyl-1-pyrroline N-oxide (DMPO) were performed to probe reactive oxygen species (ROS) generated during methylene blue degradation over the TiO_2–rGO–0.5 photocatalyst, identified as the most active composition under mechanical excitation and coupled photo-mechanical activation. The spectra (Figure 14) exhibit a characteristic four-line pattern (1:2:2:1) with hyperfine splitting constants a_N ≈1.5 mT and a_H ≈1.5 mT, and a g-value of ~2.005, consistent with a DMPO–OH adduct and indicative of hydroxyl radical-type species [43].

The spectral positions are preserved under both stirring (dark) and combined light + stirring conditions, indicating a common dominant radical pathway. Under illumination, however, additional weak features appear between the main lines, suggesting the presence of a minor secondary component, plausibly arising from superoxide-derived or surface-associated intermediates [43].

The detection of a clear EPR signal under stirring alone confirms that mechanical stimulation can induce reactive oxygen species (ROS) generation in the multiphase TiO_2–rGO system. Under

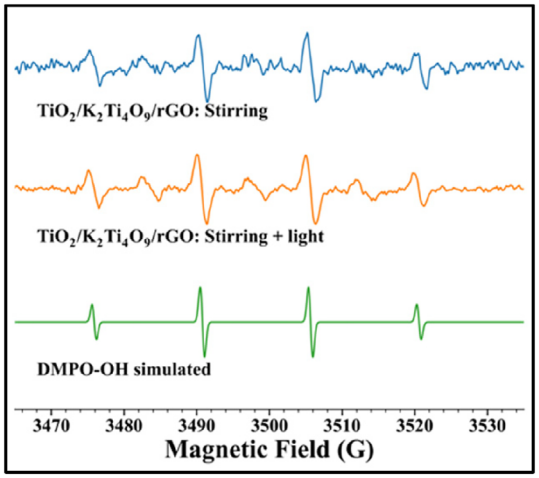

FIGURE 14 | EPR spectra of the multiphase $TiO_2/K_2Ti_4O_9$/rGO photocatalyst in methylene blue solution using DMPO as a spin-trapping agent under (i) mechanical stimulation (stirring, dark) and (ii) combined photo-mechanical activation (stirring under simulated solar irradiation). The characteristic four-line signal corresponds to a DMPO–OH spin adduct. Additional weak features observed under light suggest the presence of secondary reactive oxygen species.

simultaneous photo-mechanical activation, photogenerated carriers and strain-induced effects act cooperatively, resulting in a broader ROS distribution while maintaining the dominant hydroxyl radical-type signature.

2.7 | Proposed Photo–Mechanical Charge-Transfer Mechanism

The degradation of methylene blue over the TiO_2(B)/anatase/$K_2Ti_4O_9$/rGO composites is best described by a multiphase heterojunction mechanism involving defect-assisted visible-light excitation and rGO-mediated charge separation. Under visible-light irradiation, charge carriers are generated within the oxide domains through bandgap narrowing and interfacial/defect states associated with Ti^{3+} species and TiO_2–rGO coupling. Electrons are transferred to the rGO network, which acts as a conductive mediator, suppressing electron–hole recombination and promoting charge transport [44]. These electrons may participate in oxygen reduction pathways to form $O_2^{\bullet -}$, while holes remaining in the oxide valence bands can oxidise surface-adsorbed H_2O/OH^- to generate •OH-type species [45]. EPR spin-trapping supports •OH-type species as a dominant reactive pathway.

Under simultaneous visible-light irradiation and mechanical stirring, cyclic interfacial deformation and strain redistribution likely enhance local charge separation efficiency and reactive oxygen species generation, accelerating degradation kinetics while preserving the same fundamental reaction pathway [46]. The catalytic process can therefore be described as a coupled photo-mechanical, rGO-mediated heterojunction mechanism [47, 48]. A schematic representation of the proposed mechanism is shown in Figure 15.

3 | Conclusions

This study demonstrates a rapid, single-step continuous hydrothermal flow synthesis strategy for producing multiphase strain-engineered TiO_2–rGO nanocomposites with dual photocatalytic and mechanocatalytic activity. In situ reduction of graphene oxide under alkaline conditions induces interfacial lattice strain ($\varepsilon_{XRD} \approx 33 \times 10^{-3}$ in anatase, also evidenced by a Raman E_g shift of ~8.5 cm^{-1}) concurrently with the crystallisation of anatase TiO_2, TiO_2(B), and $K_2Ti_4O_9$. These intimate heterointerfaces facilitate efficient carrier separation and robust charge transfer to the rGO network. The resulting multiphase framework exhibits a narrowed bandgap and prolonged carrier lifetime, consistent with DFT-predicted strain-modulated band alignment.

The optimised nanocomposite achieves near-complete methylene-blue degradation (99%) within 60 min, delivering a synergy factor of $S > 1$ under simultaneous photo–mechanical activation.

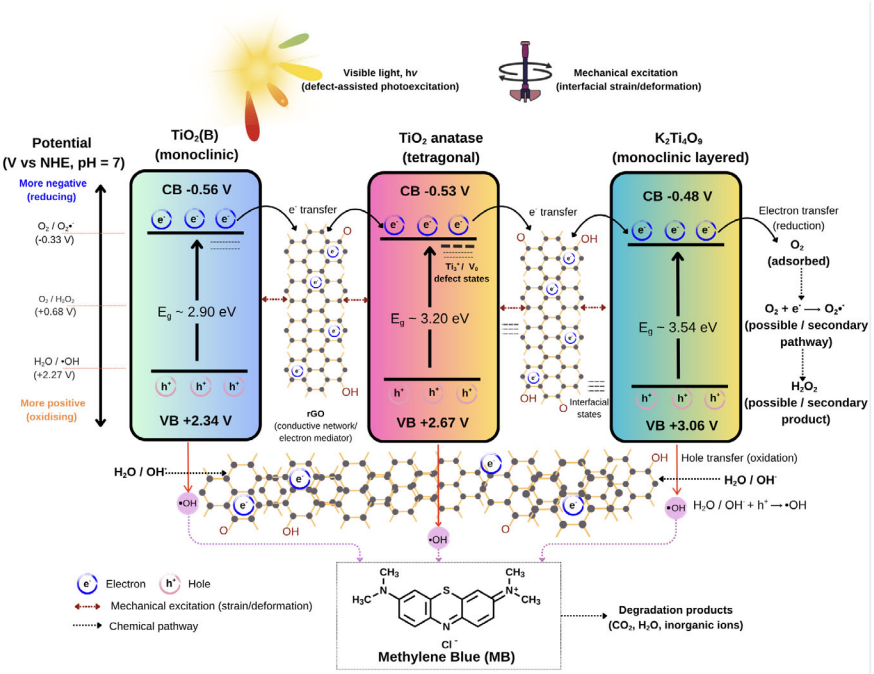

FIGURE 15 | Proposed working mechanism for methylene blue (MB) degradation over multiphase TiO_2(B)/anatase/$K_2Ti_4O_9$/rGO nanocomposites under coupled visible-range simulated solar irradiation and mechanical stirring. Under visible light, defect- and interfacial-state-assisted excitation generates charge carriers within the oxide domains. Electrons are transferred to the rGO network, which acts as a conductive mediator that facilitates electron transport and suppresses recombination. Based on the UPS-derived band alignment, these electrons may reduce dissolved oxygen to form superoxide radicals ($O_2^{\bullet -}$), while holes in the oxide valence bands oxidise surface-adsorbed H_2O/OH^- to generate hydroxyl radicals (•OH). EPR spin-trapping supports •OH-type species as the dominant reactive pathway. Mechanical stirring introduces cyclic interfacial deformation and strain re-distribution, which enhance charge separation efficiency, suppress recombination, and increase reactive oxygen species generation, leading to accelerated degradation kinetics. The schematic represents a plausible mechanism based on UPS band alignment, UV–vis absorption, PL lifetime measurements, DFT charge–transfer analysis, and EPR evidence.

The dual rate constant (0.1046 min^{-1}) compares favourably with many reported TiO_2-based systems, and the mechanocatalytic activity (5.57×10^{-3} min^{-1} at 550 rpm) is a rare demonstration of non-photonic catalysis in an oxide material. These findings demonstrate that strain-induced heterointerface coupling, validated across TEM, XRD, Raman, and DFT analyses, offers a robust mechanism for band-edge engineering and charge-transport enhancement in multiphase oxide-2D frameworks. The CHFS platform offers a scalable, sustainable route for designing multifunctional, strain-adaptive catalysts for sustainable environmental and energy conversion applications.

4 | Experimental Methodology

4.1 | Synthesis of Multiphase TiO_2-Potassium Titanate-Reduced Graphene Oxide Nanocomposites

All chemicals were used as received without further purification. Titanium(IV) bis(ammonium lactato)dihydroxide (50 wt.% in water, Sigma–Aldrich, UK) was employed as the sole titanium precursor. It was diluted with deionised water to obtain a 0.2 M aqueous solution for use in the synthesis. Graphene oxide (GO) was sourced from LayeredOne (Netherlands), and potassium hydroxide (KOH, ≥85%, Sigma–Aldrich, UK) was used as the alkaline precursor. To prepare the TiO_2-potassium titanate–reduced graphene oxide mixtures, GO was dispersed in 1.0 M KOH solution at concentrations of 0.5, 1.0, and 2.0 mg mL^{-1}. The resulting suspensions were sonicated to ensure homogeneous dispersion and subsequently stirred continuously during the synthesis process to maintain uniformity. TiO_2-based nanocomposites were synthesised using a continuous hydrothermal flow synthesis (CHFS) system operated under supercritical water conditions (Scheme 1).

Deionised water was delivered by Pump 1 at a flow rate of 20 mL min^{-1} and heated to 450°C under a pressure of 24.8 MPa to reach supercritical conditions. Pump 2 introduced the titanium precursor solution (0.2 M titanium (IV) bis (ammonium lactato) dihydroxide), while Pump 3 delivered the GO–KOH mixture at the desired concentrations. Both reagent streams were introduced at 10 mL min^{-1}. A control synthesis was also conducted using only the titanium precursor in KOH without the addition of GO. In all cases, the product stream was passed through a heat exchanger and collected downstream of the back-pressure regulator (BPR).

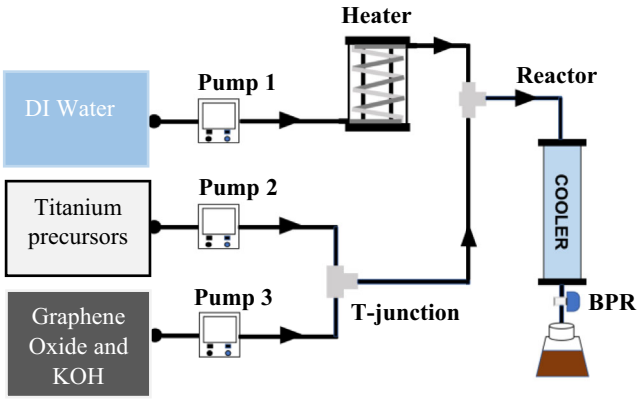

SCHEME 1 | Continuous hydrothermal flow synthesis setup used for the single-step preparation of multiphase TiO_2–rGO nanocomposites.

The resulting suspensions were cleaned via repeated centrifugation, and the recovered solids were freeze-dried to yield fine powders. The final products were denoted as TiO_2 (control, without graphene oxide), TiO_2–rGO–0.5, TiO_2–rGO–1.0, and TiO_2–rGO–2.0, corresponding to the respective GO concentrations employed. An additional reference sample was made to isolate the effect of KOH/GO and used as an unstrained benchmark for Raman analysis.

4.2 | Characterisation Techniques

High-resolution transmission electron microscopy (HRTEM) images of the synthesised TiO_2 nanocomposites were acquired using an image-aberration-corrected JEOL ARM200F microscope, operated at 200 kV acceleration voltage. Image analysis was performed using ImageJ software. Fourier Transform Infrared Spectrophotometer (IRAffinity-1S model) was used to record the FT-IR spectrum of the samplesin the range of 500 cm^{-1} to 4000 cm^{-1}. The photoluminescence (PL) lifetime measurements were conducted using Edinburgh Instrument-FLS1000 spectrometer with a 375 nm laser; the average PL lifetime was computed using exponential fitting parameters. Raman spectra of the synthesised samples were acquired using an Edinburgh Instrument RMS1000 multimodal confocal Raman microscope with a 532 nm excitation laser and a 1200 g/mm grating. X-ray diffraction (XRD) patterns were collected using an Anton Paar XRDynamic 500 powder diffractometer with a CuKα1 (1.5406 Å) Primux 300 source. Le Bail refinement was performed using FullProf software. X-ray photoelectron spectroscopy (XPS) analysis was conducted using an AXIS Ultra DLD system (Kratos Surface Analysis). The spectra were acquired using a non-monochromated Mg Kα (1253.6 eV) X-ray source operated at 144 W (12 kV × 12 mA). Ultraviolet photoemission spectroscopy (UPS) measurements were conducted using a He I (21.2 eV) radiation source integrated into a Thermo NEXSA system, with an applied bias of −9 V. UV-vis diffuse reflectance spectra of the powder samples were acquired using Shimadzu UV-2600i spectrophotometer equipped with an integrating sphere, and the optical bandgaps were estimated from Kubelka-Munk analysis. The surface area measurements of the powder synthesised samples were conducted using a Micromeritics Gemini VII instrument, employing the Brunauer–Emmett–Teller (BET) method. This S_{BET} analysis utilised a 5-point N_2 adsorption technique, and the powder samples underwent a degassing process in a FlowPrep 060 system at 180°C for 2 h. UV–vis absorbance spectra of methylene blue solutions were recorded using a Shimadzu UV-1800 spectrophotometer. The spectra were recorded in the 200–800 nm range using a quartzcuvette with a 10 mm path length. Photo-mechanical electron paramagnetic resonance (EPR) measurements were performed using a Bruker Elexsys X-band E500T continuous-wave spectrometer equipped with a Super High Sensitivity probe head. All measurements were conducted in solution at room temperature. The microwave frequency was approximately 9.8 GHz, with a microwave power of 20 mW, modulation frequency of 100 kHz, and modulation amplitude of 1 G. Samples were prepared by dispersing the photocatalyst (10.0 mg) in aqueous methylene blue

(50 mL, 0.04 mM) containing DMPO (5,5-dimethyl-1-pyrroline N-oxide, 100 mM) as a spin-trapping agent. Aliquots (50 μL) of the reaction mixture were transferred into quartz capillaries, which were then placed inside 5 mm quartz EPR tubes. All samples were positioned consistently at the centre of the resonator to ensure reproducible signal intensity. EPR spectra were recorded under different activation conditions: (i) mechanical stimulation (magnetic stirring in the dark), and (ii) combined photo-mechanical stimulation (simulated solar irradiation with simultaneous stirring). Light irradiation was provided using a MiniSol^{TM} LED solar simulator (LSH-7320, MKS Newport) operating at 1 sun intensity (100 mW cm^{-2}), with continuous stirring at 250 rpm. Control experiments were performed using methylene blue and DMPO in the absence of catalyst.

4.3 | Adsorption, Photocatalytic and Mechano catalytic Experiments

The catalytic performance of the synthesised nanocomposites was evaluated via the degradation of methylene blue (MB) [49] under both optical and mechanical excitation. In all experiments, 10.0 mg of catalyst was dispersed in 50.0 mL of MB solution (C_0 = 0.04 mM) under magnetic stirring. Photocatalytic activity was assessed under simulated solar irradiation using a MiniSol solar simulator ($\lambda \geq 400$ nm) positioned at a fixed vertical distance (27 cm) above the solution surface. The samples were stirred continuously (250 rpm), and degradation was monitored by acquiring UV–vis absorbance spectra every 10 min, with dye concentration calculated from absorbance at λ_{max} = 664 nm using a calibration curve. Photocatalytic tests were conducted at two light intensities: 1 sun (100 mW cm^{-2}) and 0.5 sun (50 mW cm^{-2}).

To account for passive dye adsorption, two control protocols were employed. First, all reaction mixtures were pre-stirred in the dark for 30 minutes to establish adsorption–desorption equilibrium prior to light or mechanical input. Second, full-duration adsorption tests were performed in the dark without stirring to verify that dye removal over the experimental time window was not due to passive adsorption alone.

Catalytic activity under mechanical excitation was assessed separately in the absence of light. The catalyst–dye suspensions were stirred at defined speeds (250, 350, 450, and 550 rpm) in complete darkness, and full UV–vis spectra were acquired every 10 minutes to determine MB degradation. This allowed the investigation of strain-activated, non-photonic catalytic pathways.

4.4 | Kinetic and Data Analysis Equations

1 The bandgap energies of the synthesised TiO_2-based nanocomposite photocatalysts were estimated using the Kubelka–Munk method (Equation (1)).

$$F(R) = \frac{K}{S} = \frac{(1-R)^2}{2R} \tag{1}$$

where R is the diffuse reflectance of the nanocomposite. The plot of $(F(R).\ h\nu)^{1/a}$ versus $h\nu$ was used to estimate the direct and indirect bandgaps of the synthesised nanocomposites, where h is Planck's constant, ν is the photon frequency, and $a = 0.5$ is used for direct bandgap estimation and $a = 2$ is used for indirect bandgap.

2 The average lifetime was determined as the intensity-weighted average of the fitted multiple exponentials:

$$\tau_{avg} = \frac{a_1\tau_1^2 + a_2\tau_2^2 + a_3\tau_3^2}{a_1\tau_1 + a_2\tau_2 + a_3\tau_3} \tag{2}$$

where a_1, a_2, a_3 are pre-exponential factors and τ_1, τ_2, τ_3 are the lifetimes of the fitted components. The average lifetime and fitting parameters are given in Table S5.

3 Kinetic analysis using the Langmuir–Hinshelwood model Equation (3), linear fits of ln (C_t/C_0 vs. time) yield apparent first-order rate constants.

$$Ln\ \frac{C_t}{C_0} = -k_{app}t \tag{3}$$

where C_0 is the initial concentration of the dye, C_t is the concentration of MB remaining at time t, t is the time of solar irradiation, and the k_{app} is the rate constant.

4 The dye adsorption capacity, q_t of the nanocomposites was investigated in the dark.

$$q_t = \frac{(C_0 - C_t) \times V \times M_{MB}}{m} \tag{4}$$

where q_t is the amount of methylene blue (MB) adsorbed per gram of the synthesised nanocomposites at a given time, C_0 is the initial concentration (0.04 mM), C_t is the concentration of *MB* remaining in the mixture at a given time, V is the volume of the solution used in the experiment (50.0 mL), and m is the mass of the photocatalyst (10.0 mg).

5 The pseudo first order equation:

$$\ln(q_e - q_t) = \ln q_e - \frac{k_1}{2.303}\ t \tag{5}$$

6 The pseudo second order equation:

$$\frac{t}{q_t} = \frac{1}{k_2\, q_e^2} + \frac{t}{q_e} \tag{6}$$

where: q_e and q_t are the adsorption capacities (mg g^{-1}) at equilibrium and at time t.

4.5 | DFT and Atomistic Calculations

Density functional theory (DFT) calculations were performed using VASP 6.3.1 with a plane-wave basis set [50–53]. Structural optimisations employed the RPBE functional within the GGA framework [54], followed by electronic structure calculations at the HSE06 level [55]. A 500 eV energy cutoff and a 0.01 eV/Å force convergence criterion were applied. Gaussian smearing of 0.03 eV was used to ensure accurate electronic occupation in semiconductors and insulators. Dispersion interactions were accounted for using the Grimme D3 correction [56]. For slab models, dipole corrections were applied along the z-direction; gamma-point sampling sufficed due to the large unit cell size [57]. Bulk calculations omitted dipole corrections but employed a $2 \times 2 \times 2$ k-point mesh.

Adsorption energies were calculated, as customary:

$$E_{ads} = E_{system} - E_{slab} - E_{adsorbate} \quad (7)$$

where E_{system}, E_{slab}, and $E_{adsorbate}$, denote the total electronic energy of the slab with the adsorbate, empty slab, and isolated adsorbate, respectively.

To investigate the strain response relevant to mechanically induced catalysis, bulk structures were compressed along various axes under two conditions: isochoric, where expansion in the perpendicular directions preserves constant volume, and static, where volume changes with no lateral relaxation. For slab models, only one dimension was varied while allowing full relaxation in the remaining directions.

Author Contributions

Kiem G Nguyen: formal analysis (lead), investigation (lead), methodology (supporting), visualisation (lead), writing – original draft (lead). **Matej Huš:** formal analysis (lead), methodology (lead), software (lead), writing – original draft (supporting), writing – review and editing (supporting). **Ana Oberlintner:** formal analysis (supporting), software (supporting), writing – review and editing (supporting). **Ioan-Alexandru Baragau:** formal analysis (supporting), investigation (supporting), writing – review and editing (supporting). **Dana G. Popescu:** formal analysis (supporting), writing – review and editing (supporting). **Daniel Gherca:** formal analysis (supporting), writing – review and editing (supporting). **Adela Nicolaev:** formal analysis (supporting), writing – review and editing (supporting). **Tobias Heil:** formal analysis (supporting), writing – review and editing (supporting). **Muhammad Tariq Sajjad:** formal analysis (supporting), funding acquisition (supporting), writing – review and editing (supporting). **Steve Dunn:** methodology (supporting), resources (supporting), writing – review and editing (supporting). **Conor Davids:** formal analysis (supporting), writing – review and editing (supporting). **Suela Kellici:** conceptualisation (lead), funding acquisition (lead), methodology (lead), project administration (lead), resources (lead), supervision (lead), writing – original draft, review and editing (lead).

Acknowledgments

S. K., K. G. N., and M. T. S. acknowledge funding from EPSRC (UKRI647), and, together with S. D., gratefully acknowledge support from LSBU. The authors thank Dr Simon Astley (Aberystwyth University) for his support with the UPS data collection, which was performed at the EPSRC National Facility ("HarwellXPS"; EP/Y023587/1, EP/Y023609/1, EP/Y023536/1, EP/Y023552/1, and EP/Y023544/1). Support from the Henry Royce Institute for Advanced Materials at Imperial College London is also acknowledged, along with access to the EPR spectrometer in SPIN-Lab, funded through EPSRC grants EP/P030548/1, EP/R00661X/1, and EP/P02520X/1. The authors also thank Dr Irena Nevjestić for technical support with the EPR measurements and Dr Floriana Tuna at University of Manchester for EPR discussions. M. H. and A. O. were supported by the Slovenian Research and Innovation Agency (ARIS) through core funding (P2-0152, J2-70085) and project funding (N2-0469). I. A. B., D. G. P., and A. N. received funding from the Core Programme of the National Institute of Materials Physics (NIMP), granted by the Romanian Authority for Research (RAR) through Project PC3-PN23080303. All photoemission experiments at NIMP were performed using the National Interest Setup "System of complex XPS/ESCA installations and research using synchrotron radiation," funded by RAR.

Funding

This work was supported by Engineering and Physical Sciences Research Council (Grant UKRI647), London South Bank University, Javna Agencija za Raziskovalno Dejavnost RS (Grants P2-0152, J2-70085, N2-0469), Autoritatea Națională pentru Cercetare Stiințifică (Grant PC3-PN23080303).

Conflicts of Interest

The authors declare no conflicts of interest.

Data Availability Statement

The data that support the findings of this study are available from the corresponding author upon reasonable request.

References

1. Y. Miao, Y. Zhao, S. Zhang, R. Shi, and T. Zhang, "Strain Engineering: A Boosting Strategy for Photocatalysis," *Advanced Materials* 34 (2022): 2200868, https://doi.org/10.1002/adma.202200868.

2. X. Liu, A. Hu, Z. Liu, et al., "Review on Fundamental and Recent Advances of Strain Engineering for Enhancing Photocatalytic CO_2 Reduction," *Advanced Energy Materials* 15 (2025): 2405320, https://doi.org/10.1002/aenm.202405320.

3. P. Bellotti and F. Glorius, "Strain-Release Photocatalysis," *Journal of the American Chemical Society* 145 (2023): 20716–20732, https://doi.org/10.1021/jacs.3c08206.

4. Z. Liu, C. Menéndez, J. Shenoy, J. N. Hart, C. C. Sorrell, and C. Cazorla, "Strain Engineering of Oxide Thin Films for Photocatalytic Applications," *Nano Energy* 72 (2020): 104732, https://doi.org/10.1016/j.nanoen.2020.104732.

5. K. G. Nguyen, M. Huš, I.-A. Baragau, et al., "Controlling the Optoelectronic Properties of Nitrogen-Doped Carbon Quantum Dots Using Biomass-Derived Precursors in a Continuous Flow System," *Carbon* 230 (2024): 119623, https://doi.org/10.1016/j.carbon.2024.119623.

6. K. G. Nguyen, M. Huš, I. Baragau, et al., "Engineering Nitrogen-Doped Carbon Quantum Dots: Tailoring Optical and Chemical Properties through Selection of Nitrogen Precursors," *Small* 20 (2024): 2310587, https://doi.org/10.1002/smll.202310587.

7. M. Nazir , K. G. Nguyen, R. T. Baker, et al. "Interfacial Strain Engineering Induces Fatigue-Resistant, High-capacity Photo-assisted Lithium Storage," *EES Batteries* 2 (2026): 849–860, https://doi.org/10.1039/d6eb00089d.

8. J. A. Darr, J. Zhang, N. M. Makwana, and X. Weng, "Continuous Hydrothermal Synthesis of Inorganic Nanoparticles: Applications and Future Directions Darr," *Chemical Reviews* 117 (2017): 11125–11238, https://doi.org/10.1021/acs.chemrev.6b00417.

9. B. You, M. T. Tang, C. Tsai, F. Abild-Pedersen, X. Zheng, and H. Li, "Enhancing Electrocatalytic Water Splitting by Strain Engineering," *Advanced Materials* 31 (2019): 1807001, https://doi.org/10.1002/adma.201807001.

10. I.-A. Baragau, J. Buckeridge, K. G. Nguyen, et al., "Outstanding Visible Light Photocatalysis Using Nano-TiO_2 Hybrids with Nitrogen-Doped Carbon Quantum Dots and/or Reduced Graphene Oxide," *Journal of Materials Chemistry A* 11 (2023): 9791–9806, https://doi.org/10.1039/D2TA09586F.

11. J. Schneider, M. Matsuoka, M. Takeuchi, et al., "Understanding TiO_2 Photocatalysis: Mechanisms and Materials," *Chemical Reviews* 114 (2014): 9919–9986, https://doi.org/10.1021/cr5001892.

12. G. H. Ahn, M. Amani, H. Rasool, et al., "Strain-Engineered Growth of Two-Dimensional Materials," *Nature Communications* 8 (2017): 608, https://doi.org/10.1038/s41467-017-00516-5.

13. E. Erusappan, S. Thiripuranthagan, M. Durai, S. Kumaravel, and D. Kim, "Development of Ultrathin 2D Layered Titanate Pt/$K_2Ti_4O_9$/rGO Nanocomposites for Enhanced Visible Active Photocatalytic Detoxification of Harmful Organic Pollutants," *Colloids and Surfaces A: Physicochemical and Engineering Aspects* 695 (2024): 134244, https://doi.org/10.1016/j.colsurfa.2024.134244.

14. F. Li, T. Shen, C. Wang, Y. Zhang, J. Qi, and H. Zhang, "Recent Advances in Strain-Induced Piezoelectric and Piezoresistive Effect-Engineered 2D Semiconductors for Adaptive Electronics and Optoelectronics," *Nano-Micro Letters* 12 (2020): 160, https://doi.org/10.1007/s40820-020-00439-9.

15. N. Meng, W. Liu, R. Jiang, et al., "Fundamentals, Advances and Perspectives of Piezocatalysis: A Marriage of Solid-State Physics and Catalytic Chemistry," *Progress in Materials Science* 138 (2023): 101161, https://doi.org/10.1016/j.pmatsci.2023.101161.

16. Y. Yang, K. Xu, B. Yang, et al., "Giant Energy Storage Density with Ultrahigh Efficiency in Multilayer Ceramic Capacitors via Interlaminar Strain Engineering," *Nature Communications* 16 (2025): 1300, https://doi.org/10.1038/s41467-025-56605-3.

17. H. Khan and M. U. H. Shah, "Modification Strategies of TiO_2 Based Photocatalysts for Enhanced Visible Light Activity and Energy Storage Ability: A Review," *Journal of Environmental Chemical Engineering* 11 (2023): 111532, https://doi.org/10.1016/j.jece.2023.111532.

18. M. Chai, B. Yuan, Y. Ban, et al., "Stable Synthesis Mechanism and Photocatalytic Properties of TiO_2 Nanocrystals with Different Morphologies Derived from Potassium Titanate Nanowires," *RSC Advances* 15 (2025): 6384–6399, https://doi.org/10.1039/D4RA08805K.

19. T. Gupta, J. Cho Samriti, and J. Prakash, "Hydrothermal Synthesis of TiO_2 Nanorods: Formation Chemistry, Growth Mechanism, and Tailoring of Surface Properties for Photocatalytic Activities," *Materials Today Chemistry* 20 (2021): 100428, https://doi.org/10.1016/j.mtchem.2021.100428.

20. S. Khan, Y. Kubota, W. Lei, et al., "One-Pot Synthesis of (anatase/Bronze-Type)-TiO_2/Carbon Dot Polymorphic Structures and Their Photocatalytic Activity for H_2 Generation," *Applied Surface Science* 526 (2020): 146650, https://doi.org/10.1016/j.apsusc.2020.146650.

21. K. Naoi, T. Kurita, M. Abe, et al., "Ultrafast Nanocrystalline-TiO_2(B)/Carbon Nanotube Hyperdispersion Prepared via Combined Ultracentrifugation and Hydrothermal Treatments for Hybrid Supercapacitors," *Advanced Materials* 28 (2016): 6751–6757, https://doi.org/10.1002/adma.201600798.

22. Y. Ide, W. Shirae, T. Takei, D. Mani, and J. Henzie, "Merging Cation Exchange and Photocatalytic Charge Separation Efficiency in an Anatase/$K_2Ti_4O_9$ Nanobelt Heterostructure for Metal Ions Fixation," *Inorganic Chemistry* 57 (2018): 6045–6050, https://doi.org/10.1021/acs.inorgchem.8b00538.

23. U. Alli, K. McCarthy, I.-A. Baragau, et al., "In-Situ Continuous Hydrothermal Synthesis of TiO_2 Nanoparticles on Conductive N-Doped MXene Nanosheets for Binder-Free Li-Ion Battery Anodes," *Chemical Engineering Journal* 430 (2022): 132976, https://doi.org/10.1016/j.cej.2021.132976.

24. H. Jo, D. H. Wi, T. Lee, et al., "Direct Strain Correlations at the Single-Atom Level in Three-Dimensional Core-Shell Interface Structures," *Nature Communications* 13 (2022): 5957, https://doi.org/10.1038/s41467-022-33236-6.

25. T. Beuvier, M. Richard-Plouet, and L. Brohan, "Accurate Methods for Quantifying the Relative Ratio of Anatase and TiO_2(B) Nanoparticles," *The Journal of Physical Chemistry C* 113 (2009): 13703–13706, https://doi.org/10.1021/jp903755p.

26. Q. Zhou, H. K. Liu, S. X. Dou, and S. Chong, "Defect-Free Prussian Blue Analogue as Zero-Strain Cathode Material for High-Energy-Density Potassium-Ion Batteries," *ACS Nano* 18 (2024): 7287–7297, https://doi.org/10.1021/acsnano.4c00251.

27. X. Liu, J. Chen, L. Yang, et al., "2D/2D g-C_3N_4/TiO_2 with Exposed (001) Facets Z-Scheme Composites Accelerating Separation of Interfacial Charge and Visible Photocatalytic Degradation of Rhodamine B," *The Journal of Physics and Chemistry of Solids* 160 (2022): 110339, https://doi.org/10.1016/j.jpcs.2021.110339.

28. W. Xie, R. Li, and Q. Xu, "Enhanced Photocatalytic Activity of Se-Doped TiO_2 under Visible Light Irradiation," *Scientific Reports* 8 (2018): 8752, https://doi.org/10.1038/s41598-018-27135-4.

29. S. Kellici, J. Acord, K. E. Moore, et al., "Continuous Hydrothermal Flow Synthesis of Graphene Quantum Dots," *Reaction Chemistry & Engineering* 3 (2018): 949–958, https://doi.org/10.1039/C8RE00158H.

30. L.-Å. Näslund and I. Persson, "XPS Spectra Curve Fittings of $Ti_3C_2T_x$ Based on First Principles Thinking," *Applied Surface Science* 593 (2022): 153442, https://doi.org/10.1016/j.apsusc.2022.153442.

31. H. Zhou, H. Wang, C. Yue, et al., "Photocatalytic Degradation by TiO_2-Conjugated/Coordination Polymer Heterojunction: Preparation, Mechanisms, and Prospects," *Applied Catalysis B: Environment and Energy* 344 (2024): 123605, https://doi.org/10.1016/j.apcatb.2023.123605.

32. B. Mulligan-Clarke, C. Davids, M. Mushtaq, et al., "Sustainable Synthesis of a High-Performing Off-stoichiometric Sodium Iron Sulfate/N-rGO Composite Cathode for Sodium-ion Batteries," *Journal of Power Sources* 668 (2026): 239320, https://doi.org/10.1016/j.jpowsour.2026.239320.

33. A. Wang, W. Yu, Y. Fang, et al., "Facile Hydrothermal Synthesis and Optical Limiting Properties of TiO_2-Reduced Graphene Oxide Nanocomposites," *Carbon* 89 (2015): 130–141, https://doi.org/10.1016/j.carbon.2015.03.037.

34. Y. Gao, K. Wang, T. Wang, et al., "Disentangling the Contribution of Surface and Bulk Ti^{3+} Defects to the Band Gap States of Rutile TiO_2 (011)," *JACS Au* 5 (2025): 1822–1832, https://doi.org/10.1021/jacsau.5c00075.

35. Z. Xiong and X. S. Zhao, "Nitrogen-Doped Titanate-Anatase Core–shell Nanobelts with Exposed {101} Anatase Facets and Enhanced Visible Light Photocatalytic Activity," *Journal of the American Chemical Society* 134 (2012): 5754–5757, https://doi.org/10.1021/ja300730c.

36. M. E. Aguirre, R. Zhou, A. J. Eugene, M. I. Guzman, and M. A. Grela, "Cu_2O/TiO_2 Heterostructures for CO_2 Reduction through a Direct Z-Scheme: Protecting Cu_2O from Photocorrosion," *Applied Catalysis B: Environmental* 217 (2017): 485–493, https://doi.org/10.1016/j.apcatb.2017.05.058.

37. A. Balapure, J. Ray Dutta, and R. Ganesan, "Recent Advances in Semiconductor Heterojunctions: A Detailed Review of the Fundamentals of Photocatalysis, Charge Transfer Mechanism and Materials," *RSC Applied Interfaces* 1 (2024): 43–69, https://doi.org/10.1039/D3LF00126A.

38. D. Kiani and I. E. Wachs, "Practical Considerations for Understanding Surface Reaction Mechanisms Involved in Heterogeneous Catalysis," *ACS Catalysis* 14 (2024): 16770–16784, https://doi.org/10.1021/acscatal.4c05188.

39. E. D. Revellame, D. L. Fortela, W. Sharp, R. Hernandez, and M. E. Zappi, "Adsorption Kinetic Modeling Using Pseudo-First Order and Pseudo-Second Order Rate Laws: A Review," *Cleaner Engineering and Technology* 1 (2020): 100032, https://doi.org/10.1016/j.clet.2020.100032.

40. U. Diebold, "The Surface Science of Titanium Dioxide," *Surface Science Reports* 48 (2003): 53–229, https://doi.org/10.1016/S0167-5729(02)00100-0.

41. L. Gong, F. Zhang, X. Peng, et al., "Improving the Damping Properties of Carbon Fiber Reinforced Polymer Composites by Interfacial Sliding of Oriented Multilayer Graphene Oxide," *Composites Science and Technology* 224 (2022): 109309, https://doi.org/10.1016/j.compscitech.2022.109309.

42. W. Xue, H. Li, R. Dugnani, et al., "High Loss Factor Piezoelectric Damping Composite with Three-Dimensional Reduced Graphene Oxide as the Conductive Phase," *RSC Advances* 8 (2018): 12494–12502, https://doi.org/10.1039/C8RA00175H.

43. L. Li, L. Shan, A. M. Sheveleva, et al., "Control of Evolution of Porous Copper-Based Metal–organic Materials for Electroreduction of CO_2 to Multi-Carbon Products," *Materials Advances* 4, no. 8 (2023): 1941–1948, https://doi.org/10.1039/D3MA00033H.

44. A. Iwase, Y. H. Ng, Y. Ishiguro, A. Kudo, and R. Amal, "Reduced Graphene Oxide as a Solid-State Electron Mediator in Z-Scheme Photocatalytic Water Splitting under Visible Light," *Journal of the American Chemical Society* 133 (2011): 11054–11057, https://doi.org/10.1021/ja203296z.

45. Y. Lu, X.-L. Liu, L. He, et al., "Spatial Heterojunction in Nanostructured TiO_2 and Its Cascade Effect for Efficient Photocatalysis," *Nano Letters* 20 (2020): 3122–3129, https://doi.org/10.1021/acs.nanolett.9b05121.

46. Y. Hu, Y. Pan, Z. Wang, et al., "Lattice Distortion Induced Internal Electric Field in TiO_2 Photoelectrode for Efficient Charge Separation and Transfer," *Nature Communications* 11 (2020): 2129, https://doi.org/10.1038/s41467-020-15993-4.

47. P. Wang, S. Fan, X. Li, et al., "Piezotronic Effect and Hierarchical Z-Scheme Heterostructure Stimulated Photocatalytic H_2 Evolution Integrated with C-N Coupling of Benzylamine," *Nano Energy* 89 (2021): 106349, https://doi.org/10.1016/j.nanoen.2021.106349.

48. R. Xu, Z. Liu, B. Xie, and L. Shu, "Lattice Strain Engineered Reactive Oxygen Species Generation of $NaNbO_3$ Ferroelectric," *Nano Energy* 127 (2024): 109738, https://doi.org/10.1016/j.nanoen.2024.109738.

49. K. Thompson, J. Goodall, S. Kellici, et al., "Screening Tests for the Evaluation of Nanoparticle Titania Photocatalysts," *Journal of Chemical Technology & Biotechnology*, 84, no. 11 (2009): 1717–1725, https://doi.org/10.1002/jctb.2237.

50. G. Kresse and J. Hafner, "Ab Initio Molecular Dynamics for Liquid Metals," *Physical Review B* 47 (1993): 558–561, https://doi.org/10.1103/PhysRevB.47.558.

51. G. Kresse and J. Hafner, "Ab Initio Molecular-Dynamics Simulation of the Liquid-Metal–amorphous-Semiconductor Transition in Germanium," *Physical Review B* 49 (1994): 14251–14269, https://doi.org/10.1103/PhysRevB.49.14251.

52. G. Kresse and J. Furthmüller, "Efficiency of Ab-Initio Total Energy Calculations for Metals and Semiconductors Using a Plane-Wave Basis Set," *Computational Materials Science* 6 (1996): 15–50, https://doi.org/10.1016/0927-0256(96)00008-0.

53. G. Kresse and J. Furthmüller, "Efficient Iterative Schemes for Ab Initio Total-Energy Calculations Using a Plane-Wave Basis Set," *Physical Review B* 54 (1996): 11169–11186, https://doi.org/10.1103/PhysRevB.54.11169.

54. B. Hammer, L. B. Hansen, and J. K. Nørskov, "Improved Adsorption Energetics Within Density-Functional Theory Using Revised Perdew–Burke–Ernzerhof Functionals," *Physical Review B* 59 (1999): 7413–7421, https://doi.org/10.1103/PhysRevB.59.7413.

55. J. Heyd, G. E. Scuseria, and M. Ernzerhof, "Hybrid Functionals Based on a Screened Coulomb Potential," *The Journal of Chemical Physics* 125 (2003): 8207–8215, https://doi.org/10.1063/1.2404663.

56. S. Grimme, J. Antony, S. Ehrlich, and H. Krieg, "A Consistent and Accurate Ab Initio Parametrization of Density Functional Dispersion Correction (DFT-D) for the 94 elements H–Pu," *The Journal of Chemical Physics* 132 (2010): 154104, https://doi.org/10.1063/1.3382344.

57. J. Neugebauer and M. Scheffler, "Adsorbate-Substrate and Adsorbate-Adsorbate Interactions of Na and K Adlayers on Al(111)," *Physical Review B* 46 (1992): 16067–16080, https://doi.org/10.1103/PhysRevB.46.16067.

Supporting Information

Additional supporting information can be found online in the Supporting Information section.